Photospheric silicon abundances of upper main-sequence stars derived from Si II 6347/6371 doublet lines

Yoichi Takeda

11-2 Enomachi, Naka-ku, Hiroshima-shi, 730-0851, Japan
(E-mail: ytakeda@js2.so-net.ne.jp)

Abstract. Silicon abundances were determined by applying the spectrum-fitting technic to the Si II doublet lines at 6347 and 6371 Å for a sample of 120 main-sequence stars in the $T_{\rm eff}$ range of $\sim$ 7000–14000 K (comprising not only normal stars but also non-magnetic chemically peculiar stars) with an aim of investigating their behaviors (e.g., correlation with stellar parameters and abundances of other elements such as Fe or C) and the background physical mechanisms involved therein, where attention was paid to taking into account of the non-LTE effect and to assigning a reasonable value of microturbulence. The following trends were revealed from the analysis: (i) The resulting [Si/H] values, mostly ranging from $\sim$ -0.5 to $\sim$ $+0.3$, show a positive correlation with [Fe/H]. (ii) A kind of anti-correlation exists between Si and C as seen from the tendency of [C/Si] steeply decreasing with [Si/H]. (iii) Si abundances do not show any clear dependence upon $T_{\rm eff}$ or $v_{\rm e} \sin i$, while Am and HgMn stars appear to show comparatively higher [Si/H] than normal stars. Although it is not straightforward to explain these observational facts, different physical processes (gas–dust separation and atomic diffusion) are likely to be intricately involved in producing these characteristic behaviors of Si composition in the surface of late A through late B dwarfs.
Key words: physical processes: diffusion – stars: abundances – stars: atmospheres – stars: chemically peculiar – stars: early-type

1. Introduction

It is known that a significant fraction of late A through late B-type main sequence stars show anomalous spectra indicative of surface abundance anomalies. Those chemically peculiar (CP) stars are divided into several groups according to their features as summarized in the review paper by Preston (1974). So far, the abundance characteristics of many elements in CP stars have been investigated in comparison with normal stars to discuss the origin of their anomalies.

However, regarding silicon, an important abundant element used as the fiducial reference in geo- or cosmo-chemistry, its abundance behavior in upper main-sequence stars is not yet well understood. While conspicuous overabundance of

Si is known to be observed in magnetic CP stars (CP2; the group 2 in CP stars classified by Preston 1974), how it behaves in non-magnetic CP stars (CP1 — Am stars; CP3 — HgMn stars) or in normal stars is not clear. As a matter of fact, we still do not know whether any Si anomaly ever exists in these stars. According to the atomic diffusion theory (see, e.g., Michaud et al. 2015), which is considered to be a promising mechanism to explain the origin of abundance characteristics in CP stars, Si is expected to be somewhat underabundant (Richer et al. 2000; Talon et al. 2006). Meanwhile, such a trend is not necessarily seen in spectroscopically determined Si abundances of A- and late B-type dwarfs, which are rather diversified around the normal (solar) abundance (somewhat overabundant or underabundant depending on cases; e.g., Niemczura et al. 2015; Ghazaryan, Alecian 2016; Mashonkina et al. 2020b; Saffe et al. 2021), though Si abundance determination significantly depends upon which line is to be used.

Another noteworthy aspect characterizing the importance of Si abundance is that this element is a typical refractory species (being easily fractionated into dust) in contrast to the volatile elements such as C, N, and O. Interestingly, Holweger and Stürenburg (1993) reported that even normal early A-type stars (like λ Boo-type stars) show anti-correlation between the abundances of Si and C ([C/Si] systematically decreases with [Si/H]), which means that some kind of gas–dust separation process (its degree being different from star to star) would have operated in the star formation phase and altered the primordial composition of gas. Is such an effect observed also stars of other types (i.e., late A through late B stars including CP1 and CP3 stars)? This is an interesting problem to be clarified.

Conveniently, Takeda et al. (2018; hereinafter referred to as T18) recently published the C, N, and O abundances for a large sample of 100 main-sequence stars (comprising normal as well as non-magnetic CP stars) covering $7000 \lesssim T_{\mathrm{eff}} \lesssim 11000$ K. It would be worthwhile, therefore, to determine the Si abundances for these stars. This would enable to clarify the behaviors of both [Si/H] and [C/Si], by which the nature of abundance peculiarity of Si (if any exists) in late A through late B-type stars and the involved physical process may be investigated. This is the aim of the present study.

In the past Si abundance determinations in upper main-sequence stars so far, it appears that neutral Si I lines were mainly used in late–mid A-type stars (including classical Am stars) while once-ionized Si II lines were primarily employed in early A and late B stars (because Si I lines quickly fade out with an increase in T_{eff}). Since the mixed use of lines of different ionization stages is not advantageous because of inevitable line-by-line abundance discrepancies (see, e.g., Mashonkina 2020a), we decided to invoke in this study only the Si II doublet lines at 6347 and 6371 Å, which are of high quality (i.e., almost free from blending) and sufficiently strong over the whole relevant T_{eff} range. Nevertheless, some disadvantages are involved in using these strong Si II lines; that is, the resulting Si abundances suffer an appreciable non-LTE affect and are

sensitive to the microturbulence parameter. Accordingly, special attention had to be paid to these two points.

2. Observational data

Regarding the program stars in this study, all the 101 targets (including the reference star Procyon) in T18 (cf. Section 2 therein) were adopted without change. In addition, in order to back up the range of $11000 \lesssim T_{\text{eff}} \lesssim 14000$ K (which was not covered in T18), 19 late B-type stars (among which $\sim 40\%$ are CP3 stars) were newly included. As such, our targets are 120 late B-type through early F-type stars on or near to the main sequence (luminosity classes of III–V) which have slow to moderately-high rotational velocities (0 km s$^{-1} \lesssim v_{\text{e}} \sin i \lesssim 100$ km s^{-1}). Among these, about $\sim 1/3$ are non-magnetic CP stars: 25 Am stars, 13 HgMn (or Mn) stars, and 2 λ Boo stars. Besides, our sample includes 16 Hyades A-type stars. The list of these 120 stars is given in Table 1, while the data source and the basic information of the observational materials are summarized in Table 2.
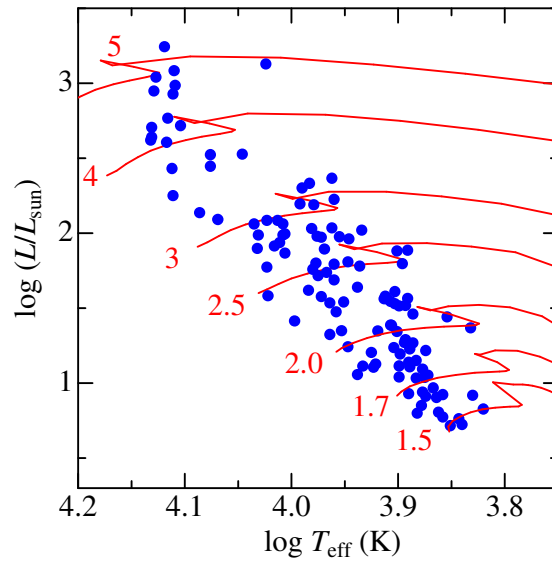
Figure 1. The 120 program stars are plotted on the theoretical HR diagram ($\log(L/L_{\odot})$ vs. $\log T_{\text{eff}}$), where T_{eff} was derived from colors (cf. Section 3) and L was evaluated from visual magnitude (corrected for interstellar extinction by following Arenou et al. 1992), Hipparcos parallax (van Leeuwen 2007), and bolometric correction (Flower 1996). Theoretical solar-metallicity tracks for 7 different masses (1.5, 1.7, 2, 2.5, 3, 4, and 5 $M_{\odot}$), which were computed by Lejeune and Schaerer (2001), are also depicted by solid lines for comparison.

Table 1. Stellar parameters and the resulting abundances of the program stars

HD# (1)	Name (2)	Sp.Type (3)	$T_{\rm eff}$ (4)	$\log g$ (5)	[Fe/H] (6)	$v_{\rm e}\sin i$ (7)	[C/H] (8)	$\xi_{\rm std}$ (9)	[Si/H]$_{\rm std}$ (10)	$\xi_{\rm refit}$ (11)	[Si/H]$_{\rm refit}$ (12)	Group (13)	Remark (14)
002628	28 And	A7III	7143	3.48	−0.27	19	−0.32	3.35	−0.27	4.27	−0.29	D	
005448	μ And	A5V	8147	3.82	−0.14	72	−0.32	3.98	−0.31	1.31	+0.22	B	
011529	ω Cas	B8III	12858	3.43	−0.15	30	$\cdots$	1.00	−0.02	$\cdots$	$\cdots$	F	SBo
011636	β Ari	A5V...	8294	4.12	+0.15	73	−0.49	3.93	−0.09	4.01	−0.02	B	SBo
012111	48 Cas	A3IV	7910	4.08	−0.23	76	−0.46	3.99	−0.27	1.26	+0.25	B	SBo
012216	50 Cas	A2V	9553	3.90	+0.15	88	−0.20	2.58	−0.29	2.27	−0.17	B	SB2
013161	β Tri	A5III	7957	3.68	−0.32	65	−0.42	4.00	−0.48	$\cdots$	$\cdots$	B	SB2o
014252	10 Tri	A2V	9023	3.64	−0.04	23	−0.53	3.27	−0.32	2.19	−0.08	D	V
016350		B9.5V	9824	3.72	−0.03	21	−0.63	2.22	−0.25	$\cdots$	$\cdots$	D	
017081	π Cet	B7IV	13063	3.72	−0.10	20	$\cdots$	1.00	+0.05	2.98	−0.18	F	SB
017093	38 Ari	A7III-IV	7541	3.95	−0.23	69	−0.46	3.81	−0.26	$\cdots$	$\cdots$	B	V
018454	4 Eri	A5IV/V	7740	4.07	+0.24	100	−0.40	3.94	+0.07	$\cdots$	$\cdots$	B	V
020149		A1Vs	9522	3.99	−0.05	21	−0.25	2.62	−0.31	2.63	−0.24	D	SB?
020320	ζ Eri	A5m	7505	3.91	−0.12	67	−0.72	3.78	−0.30	2.36	−0.03	B	SBo, Am
020346		A2IV	8824	3.56	+0.07	21	−0.47	3.50	−0.28	2.98	−0.13	D	SB?
023281		A5m	7761	4.19	+0.05	76	−0.36	3.95	−0.16	3.14	+0.02	B	Am
023408	20 Tau	B8III	12917	3.36	+0.16	30	$\cdots$	1.00	−0.74	1.39	−0.71	F	SB
023878	τ^7 Eri	A1V	8674	3.80	+0.18	25	−0.63	3.65	−0.17	3.83	−0.12	D	V?
024740	32 Tau	F2IV	6768	3.77	−0.11	21	−0.07	2.71	+0.00	4.58	−0.12	D	V
025490	ν Tau	A1V	9077	3.93	−0.05	82	−0.37	3.20	−0.41	3.19	−0.33	B	
026322	44 Tau	F2IV-V	6795	3.46	−0.15	6	−0.14	2.76	−0.20	2.68	−0.12	D	
027045	ω^2 Tau	A3m	7552	4.26	+0.36	62	−0.89	3.82	+0.10	3.63	+0.20	B	SB, Am

Table 1. Continued.

HD# (1)	Name (2)	Sp.Type (3)	T_{eff} (4)	$\log g$ (5)	[Fe/H] (6)	$v_{\mathrm{e}}\sin i$ (7)	[C/H] (8)	ξ_{std} (9)	[Si/H]$_{\mathrm{std}}$ (10)	ξ_{refit} (11)	[Si/H]$_{\mathrm{refit}}$ (12)	Group (13)	Remark (14)
027628	60 Tau	A3m	7218	4.05	+0.10	30	−1.08	3.45	+0.15	4.26	+0.12	B	SB1o, Am, H
027749	63 Tau	A1m	7448	4.21	+0.41	13	−1.30	3.73	+0.09	4.05	+0.12	B	SB1o, Am, H
027819	δ^2 Tau	A7V	8047	3.95	−0.05	45	−0.15	4.00	−0.17	4.33	−0.14	B	SB, H
027934	κ^1 Tau	A7IV-V	8159	3.84	+0.02	83	−0.17	3.98	−0.21	3.70	−0.10	B	SB?, H
027962	δ^3 Tau	A2IV	8923	3.94	+0.25	11	−0.49	3.39	−0.08	3.08	+0.03	A	SB, H
028226		Am	7361	4.01	+0.31	81	−0.37	3.63	+0.16	$\cdots$	$\cdots$	B	SB2, Am, H
028319	θ^2 Tau	A7III	7789	3.68	−0.13	68	−0.26	3.96	−0.22	3.28	−0.05	B	SB1o, H
028355	79 Tau	A7V	7809	3.98	+0.19	87	−0.39	3.97	−0.06	2.37	+0.27	B	V?, H
028546	81 Tau	Am	7640	4.17	+0.23	28	−0.44	3.88	−0.05	4.18	−0.01	B	V?, Am, H
029388	90 Tau	A6V	8194	3.88	−0.01	82	−0.18	3.97	−0.13	3.28	+0.05	B	SB1, H
029479	σ^1 Tau	A4m	8406	4.14	+0.35	56	−0.52	3.87	+0.06	4.06	+0.10	B	SBo, Am, H
029499		A5m	7638	4.08	+0.29	61	−0.44	3.88	+0.19	3.98	+0.25	B	V, Am, H
030121	4 Cam	A3m	7700	3.98	+0.27	57	$\cdots$	3.92	+0.03	3.34	+0.19	B	Am
030210		Am...	7927	3.94	+0.40	56	−1.60	4.00	+0.19	4.46	+0.20	B	SB1?, Am, H
032115		A8IV	7207	4.13	−0.06	10	−0.11	3.44	−0.10	3.90	−0.06	D	V
032537	9 Aur	F0V	6970	4.07	−0.18	20	−0.26	3.07	−0.19	4.64	−0.23	D	SBo
033204		A5m	7530	4.06	+0.18	34	−0.85	3.80	+0.01	3.12	+0.18	B	Am, H
033254	16 Ori	A2m	7747	4.14	+0.28	13	−1.33	3.94	−0.02	3.90	+0.06	B	SBo, Am, H
033641	μ Aur	A4m	7961	4.21	+0.18	79	−0.49	4.00	−0.07	0.82	+0.57	B	V, Am
038899	134 Tau	B9IV	10774	4.02	+0.00	26	$\cdots$	1.16	−0.05	1.69	−0.05	F	V
039945		A5V	7827	3.36	−0.33	22	−0.34	3.97	−0.52	2.82	−0.31	D	
040626		B9.5IV	10263	4.00	+0.20	14	−0.26	1.69	−0.08	1.12	+0.08	D	

Table 1. Continued.

HD# (1)	Name (2)	Sp.Type (3)	$T_{\rm eff}$ (4)	$\log g$ (5)	[Fe/H] (6)	$v_{\rm e}\sin i$ (7)	[C/H] (8)	$\xi_{\rm std}$ (9)	[Si/H]$_{\rm std}$ (10)	$\xi_{\rm refit}$ (11)	[Si/H]$_{\rm refit}$ (12)	Group (13)	Remark (14)
040932	μ Ori	Am...	8005	3.93	-0.12	11	-0.64	4.00	-0.35	3.45	-0.22	B	SB1o, Am, H
042035		B9V	10575	3.82	-0.16	2	-0.68	1.35	-0.56	1.09	-0.47	D	V
043378	2 Lyn	A2Vs	9210	4.09	-0.15	46	-0.27	3.03	-0.32	2.99	-0.25	B	V?
045394	16 Gem	A2Vs	8630	3.42	-0.40	23	-0.62	3.69	-0.51	3.16	-0.38	D	
047105	γ Gem	A0IV	9115	3.49	-0.03	11	-0.27	3.16	-0.39	2.58	-0.24	A	SB
048915	α CMa	A0m...	9938	4.31	$+0.45$	17	-1.09	2.08	$+0.06$	1.82	$+0.17$	A	SBo, Am
053244	γ CMa	B8II	13467	3.42	$+0.06$	36	$\cdots$	1.00	-0.13	$\cdots$	$\cdots$	F	V
054834		A9V	7273	4.21	$+0.03$	30	-0.20	3.53	-0.13	3.32	-0.03	D	
058142	21 Lyn	A1V	9384	3.74	-0.05	19	-0.45	2.81	-0.30	1.36	$+0.01$	D	V
060179	α Gem	A2Vm	9122	3.88	-0.02	19	-0.93	3.15	-0.23	2.44	-0.05	B	SB1o, Am
061421	α CMi	F5IV-V	6612	4.00	$+0.00$	9	$+0.00$	1.97	$+0.00$	2.67	$+0.00$	E	SBo
067959		A1V	9168	3.65	$+0.07$	16	-0.47	3.09	-0.24	2.90	-0.14	D	
072037	2 UMa	A2m	7918	4.16	$+0.19$	12	-1.53	3.99	-0.18	3.53	-0.06	B	Am
072660		A1V	9635	3.97	$+0.37$	5	-0.77	2.47	$+0.02$	2.31	$+0.11$	D	
074198	γ Cnc	A1IV	9381	4.11	$+0.25$	85	-0.30	2.81	-0.09	2.45	$+0.04$	B	SB
075469		A2Vs	9165	3.51	-0.08	22	-0.42	3.09	-0.31	2.49	-0.14	D	
076543	o^1 Cnc	A5III	8330	4.18	$+0.38$	91	-0.54	3.91	$+0.13$	0.50	$+0.81$	B	SB
077350	ν Cnc	A0III	10141	3.68	$+0.24$	20	-0.56	1.83	-0.34	$\cdots$	$\cdots$	C	SBo, Hg
078316	κ Cnc	B8IIIMNp	13513	3.85	$+0.33$	8	$\cdots$	1.00	$+0.02$	$\cdots$	$\cdots$	C	SB1o, Hg
079158	36 Lyn	B8IIIMNp	13535	3.72	$+1.05$	46	$\cdots$	1.00	$+0.32$	3.25	$+0.03$	C	V, Hg
079469	θ Hya	B9.5V	10510	4.20	-0.02	82	-0.30	1.42	-0.49	1.19	-0.40	B	SB
084107	15 Leo	A2IV	8665	4.31	$+0.01$	38	-0.34	3.66	-0.30	3.79	-0.24	B	

Table 1. Continued.

HD# (1)	Name (2)	Sp.Type (3)	T_{eff} (4)	$\log g$ (5)	[Fe/H] (6)	$v_{\mathrm{e}} \sin i$ (7)	[C/H] (8)	ξ_{std} (9)	[Si/H]$_{\mathrm{std}}$ (10)	ξ_{refit} (11)	[Si/H]$_{\mathrm{refit}}$ (12)	Group (13)	Remark (14)
089021	λ UMa	A2IV	8861	3.61	+0.08	52	−0.57	3.46	−0.16	3.18	−0.05	B	V
089822		A0sp...	10307	3.89	+0.47	5	−0.45	1.64	−0.07	1.49	+0.02	C	SB2o, Hg
095382	59 Leo	A5III	8017	3.95	−0.09	68	−0.29	4.00	−0.17	3.71	−0.06	B	
095418	β UMa	A1V	9489	3.85	+0.24	44	−0.63	2.67	−0.10	2.45	+0.01	B	SB
095608	60 Leo	A1m	8972	4.20	+0.31	18	−1.16	3.33	−0.05	3.50	+0.00	B	Am
098664	σ Leo	B9.5Vs	10194	3.75	−0.11	62	−0.29	1.77	−0.33	1.52	−0.22	C	SB
106625	γ Crv	B8III	11902	3.36	−0.51	37	$\cdots$	1.00	−1.49	1.63	−1.46	C	SB, Hg
116656	ζ UMa	A2V	9317	4.10	+0.28	59	−0.96	2.89	−0.06	2.74	+0.03	B	SB2o
129174	π^1 Boo	B9p MnHg	12929	4.02	−0.06	16	$\cdots$	1.00	+0.05	0.94	+0.13	C	SB, Hg
130557		B9Vsvar...	10142	3.85	+0.59	55	−0.55	1.83	−0.24	1.48	−0.11	C	
130841	α^2 Lib	A3IV	8079	3.96	−0.24	58	−1.60	3.99	−0.63	$\cdots$	$\cdots$	B	SB
140436	γ CrB	A1Vs	9274	3.89	−0.27	68	−1.34	2.95	−0.70	1.61	−0.49	B	
141795	ϵ Ser	A2m	8367	4.24	+0.25	32	−1.01	3.89	−0.11	4.62	−0.12	B	V, Am
143807	ι CrB	A0p...	10828	4.06	+0.35	3	−0.53	1.12	+0.00	0.96	+0.09	D	SB, Hg
144206	υ Her	B9III	11925	3.79	+0.01	12	$\cdots$	1.00	−0.38	0.57	−0.27	C	Hg
145389	ϕ Her	B9MNp...	11714	4.02	+0.15	11	$\cdots$	1.00	−0.35	$\cdots$	$\cdots$	C	SB1o, Hg
149121	28 Her	B9.5III	10748	3.89	+0.24	10	−0.73	1.19	−0.40	0.97	−0.31	C	Hg
150100	16 Dra	B9.5Vn	10542	3.84	−0.33	36	+0.01	1.39	−0.79	$\cdots$	$\cdots$	C	V
155763	ζ Dra	B6III	13397	4.24	+0.07	41	$\cdots$	1.00	+0.09	0.88	+0.18	F	V
158716		A1V	9214	4.30	+0.28	4	−0.57	3.03	−0.01	2.79	+0.09	D	
161701		B9V	12692	4.04	+0.85	20	$\cdots$	1.00	−0.62	$\cdots$	$\cdots$	C	SB2o, Hg
172167	α Lyr	A0Vvar	9435	3.99	−0.53	22	−0.21	2.74	−0.65	2.43	−0.54	A	V, LB

Table 1. Continued.

HD# (1)	Name (2)	Sp.Type (3)	$T_{\rm eff}$ (4)	$\log g$ (5)	[Fe/H] (6)	$v_{\rm e}\sin i$ (7)	[C/H] (8)	$\xi_{\rm std}$ (9)	[Si/H]$_{\rm std}$ (10)	$\xi_{\rm refit}$ (11)	[Si/H]$_{\rm refit}$ (12)	Group (13)	Remark (14)
173648	ζ^1 Lyr	Am	8004	3.90	+0.32	32	−0.69	4.00	+0.01	4.38	+0.03	B	SB1o, Am
173880	111 Her	A5III	8567	4.27	+0.22	72	−0.08	3.75	−0.07	3.57	+0.02	B	SB?
174567		A0Vs	9778	3.59	+0.01	10	−0.40	2.28	−0.28	1.95	−0.16	D	
176984	14 Aql	A1V	9623	3.42	+0.04	29	−0.29	2.49	−0.24	1.24	+0.06	D	V?
179761	21 Aql	B8II-III	12895	3.46	−0.11	16	$\cdots$	1.00	−0.04	$\cdots$	$\cdots$	F	V
182564	π Dra	A2IIIs	9125	3.80	+0.39	27	−0.35	3.14	−0.03	3.59	−0.03	A	
189849	15 Vul	A4III	7870	3.62	−0.08	11	−0.17	3.99	−0.36	4.09	−0.30	A	SBo
190229		B9MNp...	13102	3.46	+0.72	10	$\cdots$	1.00	−0.30	$\cdots$	$\cdots$	C	SB1, Hg
192640	29 Cyg	A2V	8845	3.86	−1.41	74	+0.08	3.48	−1.52	$\cdots$	$\cdots$	B	V, LB
193432	ν Cap	B9IV	10180	3.91	+0.02	23	−0.27	1.78	−0.12	1.47	+0.01	D	V?
193452		B9.5III/IV	10543	4.15	+0.39	3	−0.86	1.39	−0.09	1.24	−0.01	C	SB1o, Hg
195725	θ Cep	A7III	7816	3.74	+0.16	49	−0.57	3.97	−0.02	4.64	−0.04	B	SB2o
196385		A9V	6919	4.23	−0.21	15	−0.17	2.98	−0.14	4.13	−0.15	D	
196426		B8IIIp	12899	3.89	−0.10	6	$\cdots$	1.00	−0.01	$\cdots$	$\cdots$	F	
197392		B8II-III	13166	3.46	−0.01	30	$\cdots$	1.00	−0.06	$\cdots$	$\cdots$	C	SB
198639	56 Cyg	A4me...	7921	4.09	+0.02	59	−0.38	3.99	−0.23	2.39	+0.08	B	V?, Am
198667	5 Aqr	B9III	11125	3.42	+0.01	26	−0.24	1.00	−0.10	$\cdots$	$\cdots$	C	V
200499	η Cap	A5V	8081	3.95	−0.17	62	−0.31	3.99	−0.34	4.26	−0.30	B	V
201433		B9V	12193	4.24	+0.00	15	$\cdots$	1.00	+0.00	$\cdots$	$\cdots$	C	SBo
202671	30 Cap	B5II/III	13566	3.36	+0.45	25	$\cdots$	1.00	−0.22	$\cdots$	$\cdots$	C	V?
204188		A8m	7622	4.21	+0.02	36	−0.43	3.87	−0.18	2.22	+0.13	B	SBo, Am
207098	δ Cap	A5mF2 (IV)	7312	4.06	+0.21	81	−2.00	3.57	+0.02	$\cdots$	$\cdots$	B	SBo, Am

Table 1. Continued.

HD# (1)	Name (2)	Sp.Type (3)	T_{eff} (4)	$\log g$ (5)	[Fe/H] (6)	$v_{\mathrm{e}}\sin i$ (7)	[C/H] (8)	ξ_{std} (9)	[Si/H]$_{\mathrm{std}}$ (10)	ξ_{refit} (11)	[Si/H]$_{\mathrm{refit}}$ (12)	Group (13)	Remark (14)
209625	32 Aqr	A5m	7700	3.87	+0.24	7	−0.72	3.92	+0.02	4.09	+0.07	D	SB1o, Am
211236		A8/A9IV/V	7488	3.96	−0.21	13	−0.39	3.76	−0.29	4.11	−0.25	D	
212061	γ Aqr	A0V	10384	3.95	−0.08	54	−0.49	1.55	−0.42	2.48	−0.46	B	SB
214994	o Peg	A1IV	9453	3.64	+0.18	6	−0.73	2.71	−0.18	2.57	−0.09	A	V
216627	δ Aqr	A3V	8587	3.59	−0.25	79	−0.45	3.73	−0.63	3.87	−0.57	B	V
218396		A5V	7091	4.06	−0.59	41	−0.11	3.27	−0.49	3.54	−0.44	B	
219485		A0V	9577	3.81	−0.05	27	−0.38	2.55	−0.33	1.82	−0.15	D	
222345	ω^1 Aqr	A7IV	7487	3.88	−0.07	86	−0.32	3.76	−0.18	3.11	−0.02	B	SB
222603	λ Psc	A7V	7757	3.99	−0.17	56	−0.27	3.95	−0.25	2.58	+0.02	B	SB
224995	31 Psc	A6V	7779	3.64	−0.13	99	−0.23	3.96	−0.26	$\cdots$	$\cdots$	D	V

(1) HD number. (2) Bayer/Flamsteed name. (3) Spectral type taken from Hipparcos catalogue (ESA 1997). (4) Effective temperature (in K). (5) Logarithm of surface gravity ($\log g$ in dex, where g is in unit of cm s^{-2}). (6) Fe abundance relative to Procyon. (7) Projected rotational velocity (in km s^{-1}). (8) Non-LTE carbon abundance relative to Procyon determined by Takeda et al. (2018). (9) Standard microturbulent velocity (in km s^{-1}) derived by Equation (1). (10) Non-LTE silicon abundance relative to Procyon corresponding to ξ_{std}. (11) Directly determined microturbulence (in km s^{-1}) as a result of spectrum refitting. (12) Non-LTE silicon abundance relative to Procyon corresponding to ξ_{refit}. (13) Group of the data source (cf. Table 2). (14) Specific remark [spectroscopic binary (SB, "o" denotes the case where orbital elements are available) or radial velocity variable (V), chemical peculiarity type (Am or HgMn or λ Boo), membership of Hyades cluster (H)]. The assigned CP classes were determined by consulting the spectral classifications in three sources: Hipparcos catalogue (ESA 1997), Bright Star Catalogue (Hoffleit, Jaschek 1991), and SIMBAD.

Table 2. Basic information of the observational data.

Group	#Instr.	Obs. Time	Resolution	Number	Star Type	Reference
†A	HIDES	2008 Oct	100000	7	A type	Takeda et al. (2012)
B	BOES	2008 Jan/Sep, 2009 Jan	45000	56	A type	Takeda et al. (2008, 2009)
C	HIDES	2012 May	70000	8	late B type	Takeda et al. (2014)
D	HIDES	2017 Aug/Nov	100000	29	A type	Takeda et al. (2018)
E	HIDES	2001 Feb	70000	1	Procyon	Takeda et al. (2005a)
F	HIDES	2006 Oct	70000	19	late B type	Takeda et al. (2010)

†Only for HD 172167 (Vega), Takeda et al.'s (2007) OAO/HIDES spectrum of high-S/N ($\sim$ 2000) and high-resolution ($\sim$ 100000) observed in 2006 May was adopted.
#HIDES and BOES denote "HIgh Dispersion Echelle Spectrograph" at Okayama Astrophysical Observatory and "Bohyunsan Observatory Echelle Spectrograph" at Bohyunsan Optical Astronomy Observatory, respectively.

3. Stellar parameters

As in T18, the effective temperature (T_{eff}) and the surface gravity ($\log g$) for each star were determined from colors of Strömgren's $uvby\beta$ photometric system by using Napiwotzki et al.'s (1993) calibration.

Especially important parameter we should care about is the microturbulence (ξ). We basically adopted (as done in T18) the analytical T_{eff}-dependent relation derived by Takeda et al. (2008)

$$\xi = 4.0 \exp\{-[\log(T_{\mathrm{eff}}/8000)/A]^2\} \tag{1}$$

(where $A \equiv [\log(10000/8000)]/\sqrt{\ln 2}$, ξ is in km s^{-1}, and T_{eff} is in K) for stars with $T_{\mathrm{eff}} < 11000$ K, while $\xi = 1$ km s^{-1} was assumed at $T_{\mathrm{eff}} > 11000$ K (where this equation yields $\xi < 1$ km s^{-1}). Such formula-based values are called as the "standard" microturbulence (designated as ξ_{std}) in order to clarify the difference from another choice of microturbulence described later (cf. Section 6.2).

The only exception is the standard star Procyon (HD 61421),[1] for which we used Takeda et al.'s (2005b) spectroscopically determined values ($T_{\mathrm{eff}} = 6612$ K,

---

[1] The reason why Procyon was chosen as the reference standard (as done in our previous studies) is to carry out abundance determination by "differential analysis" where the resulting relative abundances are unaffected by uncertainties in the gf values of spectral lines. That is, Procyon (F5 IV–V) is more suitable than the Sun (whose T_{eff} is too low in comparison with those of A and late B stars to be used for such a purpose), while its chemical abundances are

$\log g = 4.00$, and $\xi_{\rm std} = 1.97$ km s^{-1}) to maintain consistency with Takeda et al. (2008).

The adopted values of $T_{\rm eff}$, $\log g$, [Fe/H],[2] and $\xi_{\rm std}$ are summarized in Table 1. All the program stars are plotted on the $\log L$ vs. $\log T_{\rm eff}$ diagram (theoretical HR diagram) in Fig. 1, where theoretical evolutionary tracks corresponding to different stellar masses are also depicted. This figure indicates that the masses of our sample stars are in the range between $\sim 1.5 M_\odot$ and $\sim 5 M_\odot$. More detailed data regarding the targets and their stellar parameters are given in the electronic table (tableE.dat) available online at

https://www.astro.sk/caosp/Eedition/FullTexts/vol52no1/pp5-31.dat/.

The model atmosphere corresponding to each star was constructed by interpolating Kurucz's (1993a) ATLAS9 model grid (for $\xi = 2$ km s^{-1}) in terms of $T_{\rm eff}$, $\log g$, and [Fe/H].

4. Non-LTE calculation for Si

The statistical-equilibrium calculations for silicon atom were carried out by using the non-LTE code described in Takeda (1991). The atomic model of Si adopted in this study was constructed based on Kurucz and Bell's (1995) compilation of atomic data (gf values, levels, etc.), which consists of 34 Si I terms (up to $4d$ ^{1}F$^{\rm o}$ at 58893.4 cm^{-1}) with 222 Si I radiative transitions, 31 Si II terms (up to $3p^3$ ^{4}S$^{\rm o}$ at 123033.5 cm^{-1}) with 109 Si II radiative transitions, and 23 Si III terms (up to $4p$ ^{3}P at 248073 cm^{-1}; included only for conservation of total Si atoms).

Regarding evaluations of photoionization rates, the cross-section data taken from TOPbase (Cunto, Mendoza 1992) were used for the lower 10 Si I terms and 10 Si II terms (while hydrogenic approximation was assumed for higher terms). As to the collisional rates, the theoretical results of Aggarwal and Keenan (2014) were invoked for the bound–bound electron impact rates between the lower 10 Si II terms. Otherwise, the recipe described in Sect. 3.1.3 of Takeda (1991) was followed (inelastic collisions due to neutral hydrogen atoms were formally included as described therein, though insignificant in the atmosphere of early-type stars under question).

The calculations were done on a grid of 44 ($= 11 \times 4$) solar-metallicity ([Fe/H] $= 0$) model atmospheres resulting from combinations of eleven $T_{\rm eff}$ values (6500, 7000, 7500, 8000, 8500, 9000, 9500, 10000, 11000, 12000, 13000, and 14000 K) and four $\log g$ values (3.0, 3.5, 4.0, and 4.5) while assuming $\xi = 2$ km s^{-1} and the Si abundance of $A({\rm Si}) = 7.55$ (solar Si abundance adopted in ATLAS9 models).

---

practically the same as those of the Sun (cf. the references quoted in Section IV(c) of Takeda et al. 2008).

[2] These Fe abundances were already established in our previous papers (cf. the references given in Table 2) based on the spectrum-fitting method in the wavelength region (~ 20–30Å wide) centered around ~ 6155Å (where the Fe II 6147/6149 doublet lines are the important indicators of Fe abundance).

The depth-dependent non-LTE departure coefficients to be used for each star were then evaluated by interpolating this grid in terms of $T_{\rm eff}$ and $\log g$.

5. Abundance determination

The non-LTE Si abundances were determined (as done in T18 for CNO abundances) based on Takeda's (1995) numerical algorithm by accomplishing the best fit between the synthetic and observed spectra in the 6340–6380 Å region while varying the abundances of Si and some other elements showing appreciable lines (especially Fe, plus other elements such as Mg, Mn, Zn depending on cases), $v_{\rm M}$ (macrobroadening velocity corresponding to instrumental/rotational broadening and macroturbulence) and $\Delta\lambda$ (radial velocity or wavelength shift) but the microturbulence being fixed at $\xi_{\rm std}$. Since the relevant wavelength region of the raw spectra is more or less contaminated by weak telluric lines, they were removed in advance by dividing by the spectrum of a rapid rotator as demonstrated in Fig. 2. The atomic data of spectral lines comprising in this region were exclusively taken from Kurucz and Bell's (1995) compilation (those of relevant Si II doublet lines are summarized in Table 3), though some pre-adjustments[3] were necessary in order to achieve an satisfactory fit. The accomplished fit in the neighborhood of both lines for each star is displayed in Fig. 3.

Table 3. Adopted atomic data of Si II 6347 and 6371 lines.

Multiplet No.	λ (Å)	$\chi_{\rm low}$ (eV)	$\log gf$ (dex)	Gammar (dex)	Gammas (dex)	Gammaw (dex)
2	6347.109	8.121	+0.297	9.09	−5.04	(−7.68)
2	6371.371	8.121	−0.003	9.08	−5.04	(−7.68)

Note.
These data are were taken from Kurucz and Bell's (1995) compilation, while those parenthesized are the default values calculated by Kurucz's (1993a) WIDTH9 program.
Followed by first four self-explanatory columns, damping parameters are given in the last three columns:
Gammar is the radiation damping width (s^{-1}), $\log\gamma_{\rm rad}$.
Gammas is the Stark damping width (s^{-1}) per electron density (cm^{-3}) at 10^4 K, $\log(\gamma_{\rm e}/N_{\rm e})$.
Gammaw is the van der Waals damping width (s^{-1}) per hydrogen density (cm^{-3}) at 10^4 K, $\log(\gamma_{\rm w}/N_{\rm H})$.

---

[3] Six lines (Ca I 6343.308, Si I 6353.360, Fe I 6353.835, Si I 6356.321, Ca I 6361.786, and Fe I 6368.620) included in this database were neglected, while the $\log gf$ of Fe I 6358.631 was changed from −1.04 to −1.70.

   Then, the equivalent widths (W_{6347} and W_{6371}) of the Si II 6347 and 6371 lines were inversely evaluated from the best-fit solution of $A_{std}^N(\text{Si})$ with the same model and atmospheric parameters as used in the spectrum-fitting analysis. From such evaluated W, the non-LTE abundance (A^N), LTE abundance (A^L) and non-LTE correction ($\Delta \equiv A^N - A^L$) were derived for each line. Besides, W can be further used to estimate the abundance uncertainties due to typical ambiguities of atmospheric parameters by perturbing the standard values interchangeably. Such derived W_{6347}/W_{6371} (equivalent widths), $\Delta_{6347}/\Delta_{6371}$ (non-LTE corrections), A_{std}^N (non-LTE Si abundance), $\delta_{T\pm}$ (abundance changes for T_{eff} perturbations by $\pm 3\%$), $\delta_{g\pm}$ (abundance changes for $\log g$ perturbations by ± 0.1 dex), and $\delta_{\xi\pm}$ (abundance changes for ξ perturbations by $\pm 30\%$) are plotted against T_{eff} in Fig. 4.

   These standard abundances, expressed in the form of $[\text{Si/H}]_{std}$ ($\equiv A_{std}^N(\text{star}) - A_{std}^N(\text{Procyon})$) are given in Table 1. More complete results including W and Δ are presented in "tableE.dat" of the online material.
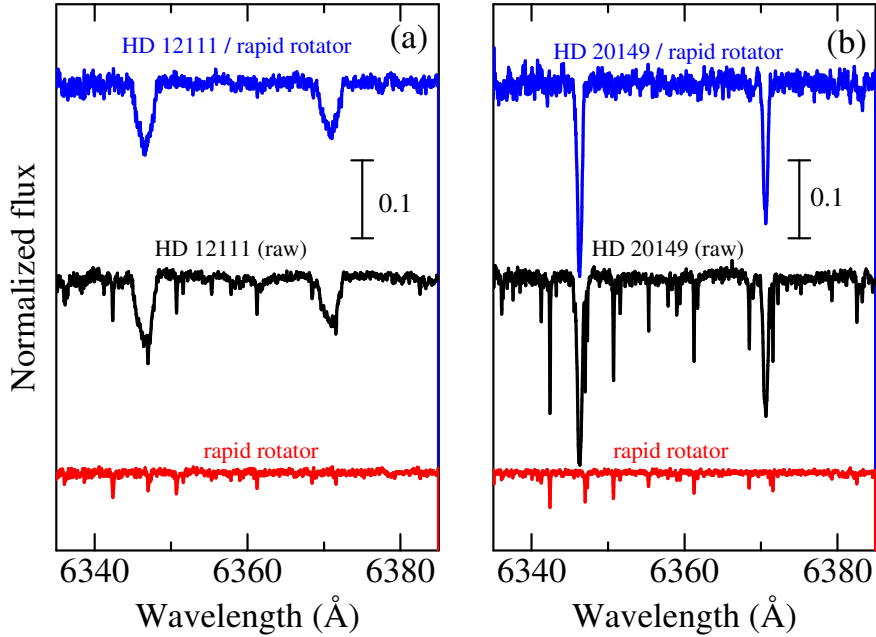
Figure 2. Examples of how the telluric lines (mostly due to H_2O vapor) are removed in the 6340–6380 Å region comprising Si II 6347/6371 lines. Dividing the raw stellar spectrum (middle, black) by the spectrum of a rapid rotator (bottom, red) results in the final spectrum (top, blue). The left (a) and right (b) panel show the cases of HD 12111 (weaker telluric contamination) and HD 20149 (stronger contamination), respectively. No Doppler correction is applied to the wavelength scale of these spectra.
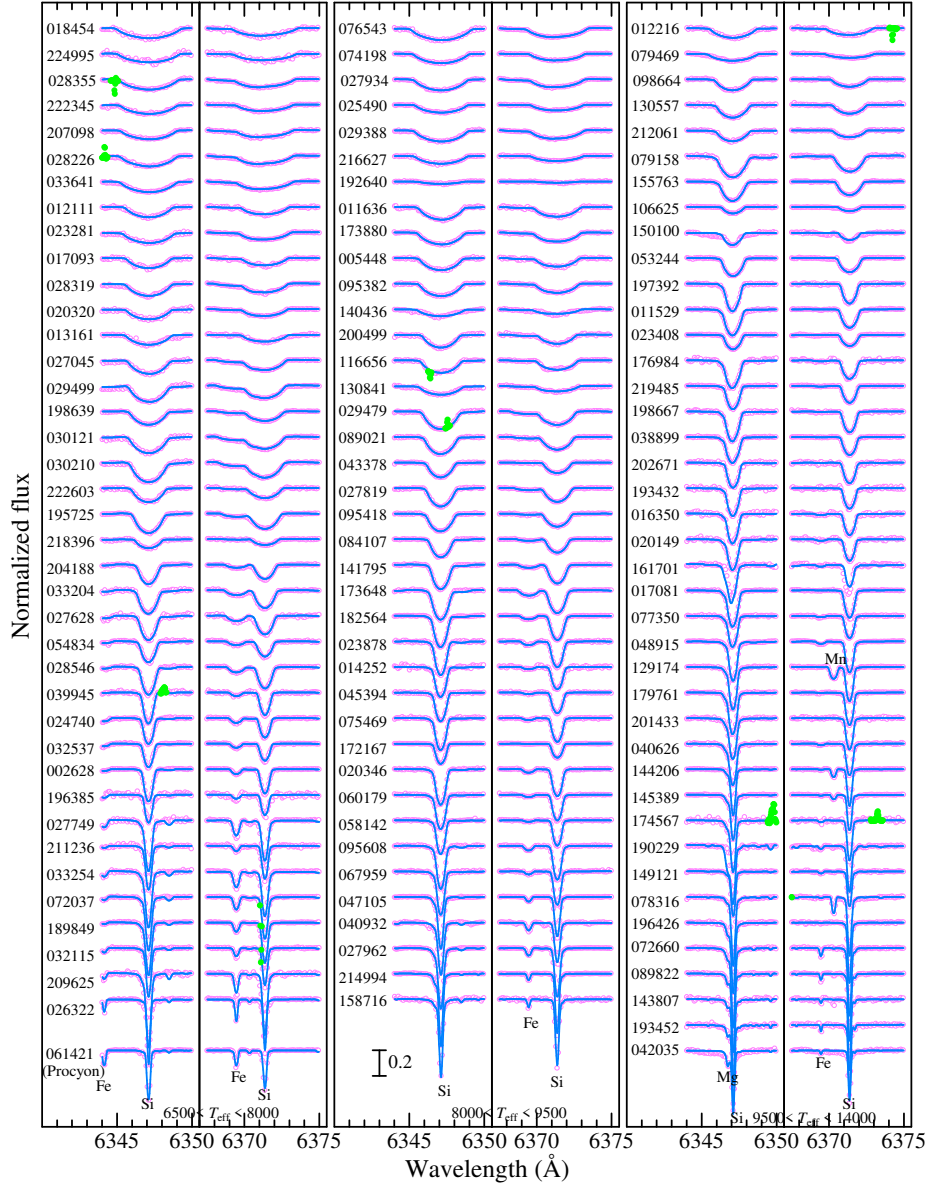
Figure 3. Synthetic spectrum fitting analysis for Si abundance determination from Si II 6347/6371 lines, In the left, middle, and right panels are shown the results for 40 stars in 6500 K < $T_{\rm eff}$ < 8000 K, 39 stars in 8000 K < $T_{\rm eff}$ < 9500 K, and 41 stars in 9500 K < $T_{\rm eff}$ < 14000 K, respectively. The best-fit theoretical spectra (in the selected ranges of 6344–6350 Å and 6367.5–6375 Å comprising the relevant Si II lines) are depicted by blue solid lines, while the observed data are plotted by pink symbols (the masked data excluded in judging the goodness of fit are highlighted in green). In each panel, the spectra are arranged in the descending order of $v_{\rm e}\sin i$, and an offset of 0.2 is applied to each spectrum (indicated by the HD number) relative to the adjacent one. The case of Procyon (standard star) is separately displayed at the bottom of the left panel.
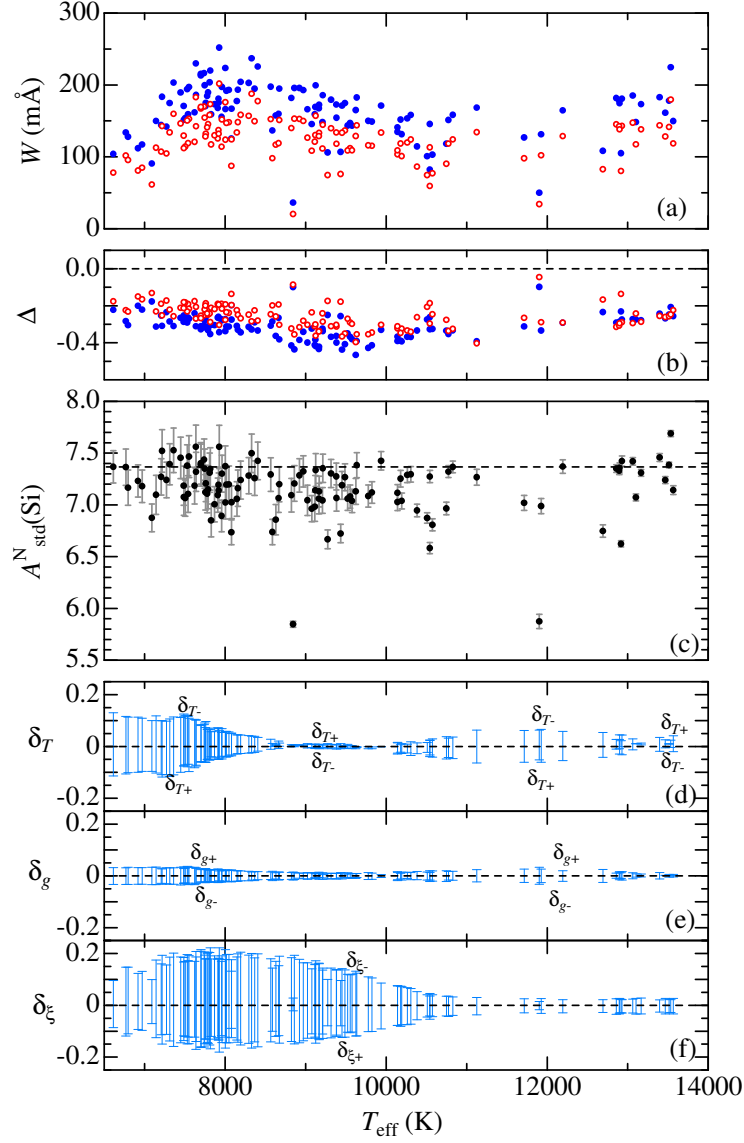
Figure 4. Silicon abundances and the related quantities plotted against $T_{\rm eff}$. (a) Equivalent widths of Si II 6347 (W_{6347}, filled symbols) and Si II 6371 (W_{6371}, open symbols). (b) Non-LTE corrections for Si II 6347 (Δ_{6347}, filled symbols) and Si II 6371 (Δ_{6371}, open symbols) (c) $A_{\rm std}^{\rm N}(\rm Si)$ (standard non-LTE Si abundance corresponding to $\xi_{\rm std}$), where the error bar denotes $\pm\delta_{Tgv}$ (root-sum-square of δ_T, δ_g, and δ_ξ, where δ_T is the mean of $|\delta_{T+}|$ and $|\delta_{T-}|$; etc.), (d) δ_{T+} and δ_{T-} (abundance variations for Si II 6347 in response to $T_{\rm eff}$ changes of $+3\%$ and -3%), (e) δ_{g+} and δ_{g-} (abundance variations for Si II 6347 in response to $\log g$ changes by $+0.1$ dex and -0.1 dex), and (f) $\delta_{\xi+}$ and $\delta_{\xi-}$ (abundance variations for Si II 6347 in response to perturbing the $\xi_{\rm std}$ value by $+30\%$ and -30%). The abundance of Procyon ($A_{\rm std}^{\rm N} = 7.367$), which is adopted as the reference, is indicated by the horizontal dashed line in panel (c).

6. Discussion and conclusion

6.1. Characteristics of the non-LTE effect

As seen from the results derived in Section 5, the Si II 6347/6371 lines suffer an appreciable non-LTE effect. According to Fig. 4b, their non-LTE abundance corrections (Δ) are negative (which means that the non-LTE effect strengthens the lines) and typically a few tenths dex ($|\Delta_{6347}| \sim 0.2$–0.5 dex, $|\Delta_{6371}| \sim 0.1$–0.4 dex; naturally the former is larger because of the stronger line forming in comparatively shallower layer). The maximum of $|\Delta|$ is around $T_{\rm eff} \sim 10000$ K.
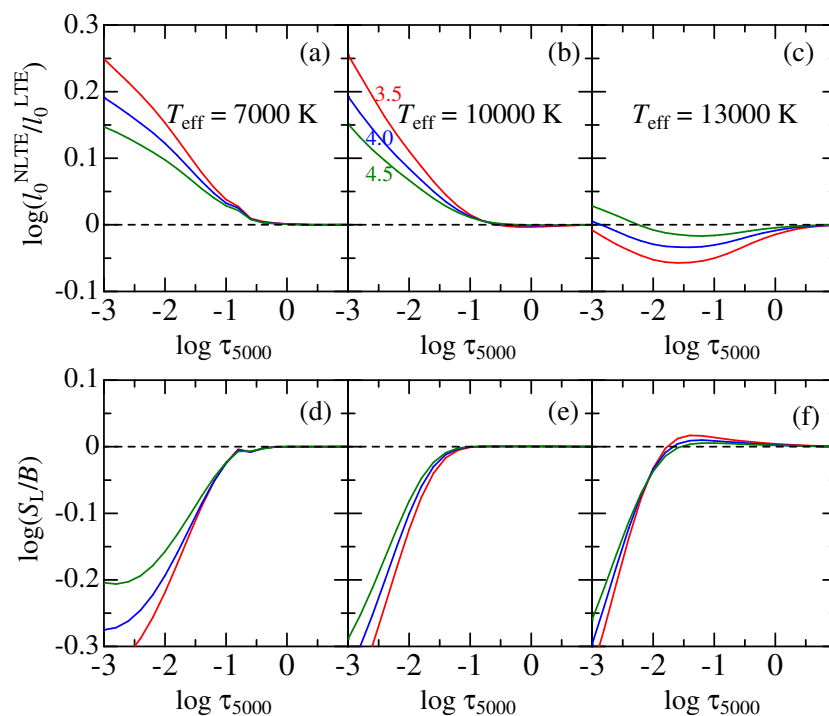
Figure 5. The non-LTE-to-LTE line-center opacity ratio (upper panels a–c) and the ratio of the line source function ($S_{\rm L}$) to the local Planck function (B) (lower panels d–f) for the Si II 4s ^{2}S–4p ^{2}P$^{\rm o}$ transition (corresponding to Si II 6347/6371 lines) of multiplet 2, plotted against the continuum optical depth at 5000 Å. Computations were done with $\xi = 2$ km s^{-1} on the solar-metallicity models ([Fe/H] = [Si/Fe] = 0) of $T_{\rm eff}$ = 7000 K (left panels a, d), 10000 K (middle panels b, e), and 13000 K (right panels c, f). At each panel are shown the results for three $\log g$ values of 3.5, 4.0, and 4.5 depicted by different colors (red, blue, and green, respectively).
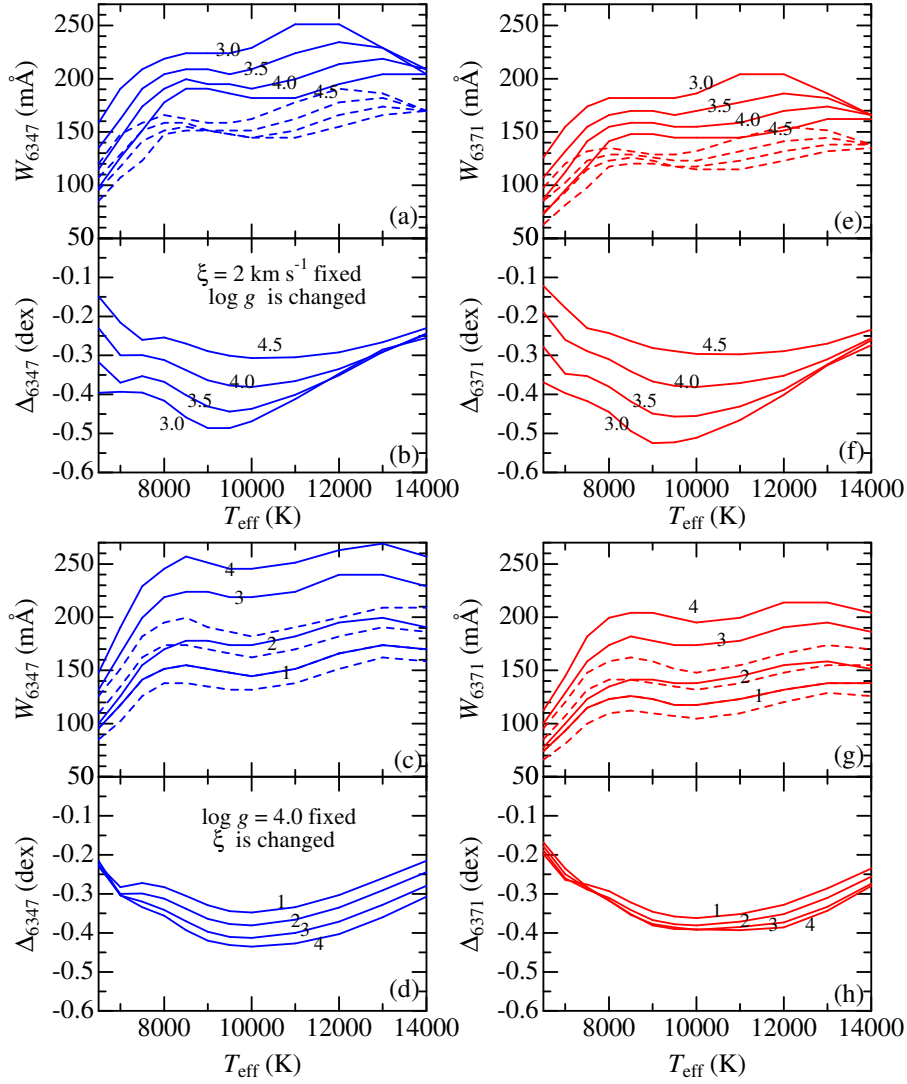
Figure 6. The non-LTE and LTE equivalent widths (W^{N} and W^{L}) for the Si II 6347/6371 lines and the corresponding non-LTE corrections (Δ), which were computed on the non-LTE grid of models described in Section 4, are plotted against T_{eff}. Each figure set consists of two panels; the upper panel is for W^{N} (solid lines) and W^{L} (dashed lines), while the lower panel is for Δ. The upper sets (a+b, e+f) show the case of fixed ξ (2 km s^{-1}) but different $\log g$ (3.0, 3.5, 4.0, and 4.5), while the lower sets (c+d, g+h) are for the case of fixed $\log g$ (4.0) but different ξ (1, 2, 3, and 4 km s^{-1}). The left-hand figures show the results for the Si II 6347 line, while the right-hand ones for the Si II 6371 line.

In Fig. 5 are shown the $l_0^{\mathrm{NLTE}}(\tau)/l_0^{\mathrm{LTE}}(\tau)$ (the non-LTE-to-LTE line-center opacity ratio; almost equal to $\simeq b_1$) and $S_{\mathrm{L}}(\tau)/B(\tau)$ (the ratio of the line source function to the Planck function; nearly equal to $\simeq b_2/b_1$) for the transition relevant to the Si II 6347/6371 lines (b_1 and b_2 are the non-LTE departure coefficients for the lower and upper terms), which were computed on the models of representative T_{eff} and $\log g$ values. As seen from this figure, while $l_0^{\mathrm{NLTE}}/l_0^{\mathrm{LTE}} > 1$ (overpopulation) holds in the line-forming region at $T_{\mathrm{eff}} \lesssim 10000$ K (A-type tars), this inequality suddenly turns to be reversed (underpopulation) at higher T_{eff} (late B-type stars) because of the beginning of Si II overionization (once-ionized Si is not the dominant ionization stage any more in such a higher T_{eff} regime). Although the non-LTE effect still acts to intensify lines (Δ remains negative) at 10000 K $\lesssim T_{\mathrm{eff}} \lesssim 14000$ K due to the dilution of $S_{\mathrm{L}}(< B)$ (see the lower panels in Fig. 5), $|\Delta|$ progressively decreases with an increase in T_{eff} (see also the Appendix A where the behavior of Δ in B-type stars is further discussed).

How the theoretical W and Δ computed for these two Si II lines depend upon the atmospheric parameters (T_{eff}, $\log g$, and ξ) is illustrated in Fig. 6, which reasonably explains the trends observed in Figs. 4a and 4b (the maximum of W is seen around $T_{\mathrm{eff}} \sim 8000$ K because the peak of ξ is attained there).

6.2. Consistency check of microturbulence

As is evident from the lower three panels (d–f) of Fig. 4, an uncertainty ξ has the most significant impact on the Si abundance among the three atmospheric parameters especially at $T_{\mathrm{eff}} \lesssim 10000$ K, since the Si II 6347/6371 lines are strong and saturated (on the flat part of the curve of growth). Therefore, particular attention should be paid to whether or not an appropriate choice of ξ has be done. As a matter of fact, Takeda et al. (2009) reported that considerably underestimated Na abundance would result from the strongly saturated Na I 5889/5895 D lines if the microturbulence given by Equation (1) is used, which may be attributed to the depth-dependence of ξ (cf. Section 5 therein) Does such an inadequacy similarly exist also for the case of Si II 6347/6371 lines?

In order to examine this problem, another solution of microturbulence was determined from these doublet lines themselves by taking the advantage that their $\log gf$ strengths are different by 0.3 dex. That is, spectrum fitting analysis was retried (taking $A_{\mathrm{std}}^{\mathrm{N}}$ and ξ_{std} as the starting solutions) while allowing *both* $A^{\mathrm{N}}(\mathrm{Si})$ and ξ to vary. These refit solutions (which are referred to as $A_{\mathrm{refit}}^{\mathrm{N}}$ and ξ_{refit}) were successfully converged for 97 stars (about $\sim 80\%$), though failed for the remaining 23 stars.

The resulting $A_{\mathrm{refit}}^{\mathrm{N}}$ and ξ_{refit} (given in Table 1) are compared with $A_{\mathrm{std}}^{\mathrm{N}}$ and ξ_{std} in Fig. 7, where the following characteristics are observed.
— Fig. 7a indicates that consistency between ξ_{refit} (dots) and ξ_{std} (solid line) is not necessarily bad, though considerable discrepancy (quite a few ξ_{refit} values
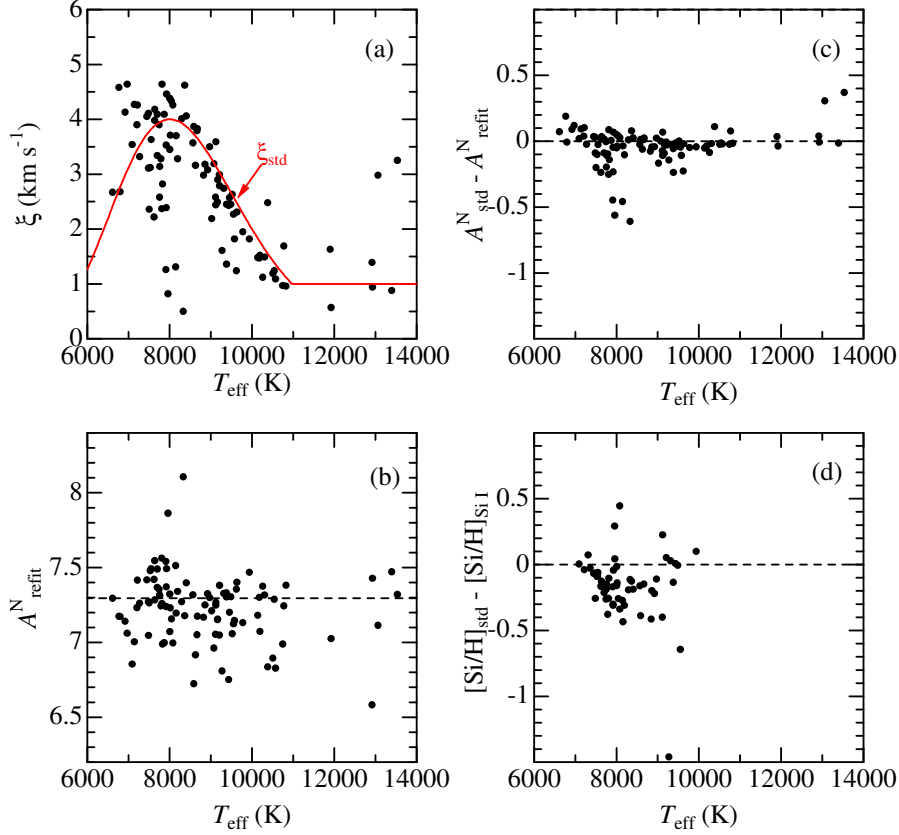
Figure 7. (a) Microturbulence directly determined by spectrum refitting (ξ_{refit}) plotted against T_{eff} by dots, while the T_{eff}-dependent standard microturbulence (ξ_{std}) given by Equation (1) is shown by the red solid line. (b) Non-LTE Si abundance ($A_{\mathrm{refit}}^{\mathrm{N}}$) resulting from refitting (corresponding to ξ_{refit}) plotted against T_{eff}. (c) Difference between "std" and "refit" abundances ($A_{\mathrm{std}}^{\mathrm{N}} - A_{\mathrm{refit}}^{\mathrm{N}}$) plotted against T_{eff}. (d) Difference between $[\mathrm{Si/H}]_{\mathrm{std}}$ (derived in this study based on Si II 6347/6371 lines by using the standard ξ_{std}) and $[\mathrm{Si/H}]_{\mathrm{Si\,I}}$ (derived by Takeda et al. 2009) based on the spectrum fitting applied to the region comprising Si I lines) plotted against T_{eff}.

tending to be appreciably lower than ξ_{std}) is seen around $T_{\mathrm{eff}} \sim 8000$ K.[4]
— As a result, $A_{\mathrm{std}}^{\mathrm{N}}$ tends to be lower than $A_{\mathrm{refit}}^{\mathrm{N}}$ at $T_{\mathrm{eff}} \sim 8000$ K. The differences are typically a few tenths dex (four stars show especially large discrepancies of

---

[4] Besides, two ξ_{refit} values around $T_{\mathrm{eff}} \sim 13000$ K are apparently two large; but they are not reliable and should not be seriously taken, because determination becomes more difficult for the case of weaker Si II lines at higher T_{eff}.

$\sim$ 0.5–0.6 dex (cf. Fig. 7c).

— It is worth noting that the $[\mathrm{Si/H}]^{\mathrm{N}}_{\mathrm{std}}$ values also exhibit similar discrepancies when compared with Takeda et al.'s (2009) [Si/H] results derived from the spectrum fitting in the 6140–6170 Å region comprising Si I lines (Fig. 7d).

— Accordingly, we may state that the abundances derived from Si II 6347/6371 lines by using Equation (1)-based ξ_{std} are apt to be underestimated around $T_{\mathrm{eff}} \sim$ 8000 K corresponding to late-to-mid A-type stars.

— However, this problem is not so serious as the case of Na I 5889/5895 lines addressed by Takeda et al. (2009). Actually, the appearance of $A^{\mathrm{N}}_{\mathrm{refit}}$ vs. T_{eff} plot (Fig. 7b) is not significantly different from the case of $A^{\mathrm{N}}_{\mathrm{std}}$ (Fig. 4c). In the figures illustrating the behaviors of Si abundances to be discussed in the next section, both ("std" and "refit") results will be shown, so that they may be compared with each other.

6.3. Observed trend of Si abundances

The relative abundances of Si ([Si/H]) and the C-to-Si ratios ([C/Si] = [C/H] − [Si/H]) for the 120 stars are plotted against the stellar parameters (and the corresponding [C/H] or [Si/H]) in Fig. 8, where two kinds of results based on $A^{\mathrm{N}}_{\mathrm{std}}$ and $A^{\mathrm{N}}_{\mathrm{refit}}$ are presented in parallel in each panel. Besides, the same correlation plots as Fig. 8 but only for the selected 16 Hyades stars are depicted in Fig. 9. The following characteristics can be read from these figures.

- The resulting Si abundances (relative to Procyon) for most stars are in the range of $-0.5 \lesssim [\mathrm{Si/H}] \lesssim +0.3$ (tending to be rather Si-deficient than Si-rich).

- As for the relation to stellar parameters, any clear dependence upon T_{eff} or $v_{\mathrm{e}}\sin i$ is not observed in [Si/H] (Figs. 9a and 9b).

- Am stars and HgMn stars appear to show somewhat higher [Si/H] than normal stars, while λ Boo stars are naturally Si-deficient. The mean $[\mathrm{Si/H}]_{\mathrm{std}}$ values for each star group are -0.23 (normal), -0.03 (Am), -0.18 (HgMn),[5] and -1.08 (λ Boo).

- A positive correlation exists between [Si/H] and [Fe/H] (Fig. 8c), which is also observed for the selected sample of Hyades stars (Fig. 9c). Actually, the correlation coefficients calculated between $[\mathrm{Si/H}]_{\mathrm{std}}$ and [Fe/H] are $+0.65$ (all sample) and $+0.82$ (Hyades sample).

- The C-to-Si ratio ([C/Si]) tends to decrease systematically with an increase in [Si/H] (Fig. 8h) indicating that C and Si are anti-correlated, though the nature of anti-correlation between [Si/H] and [C/H] is not very clear (Fig. 8d).

[5] HD 106625 (γ Crv) was excluded in the averaging process because of its exceptionally low $[\mathrm{Si/H}]_{\mathrm{std}}$ of -1.49 for this HgMn group.
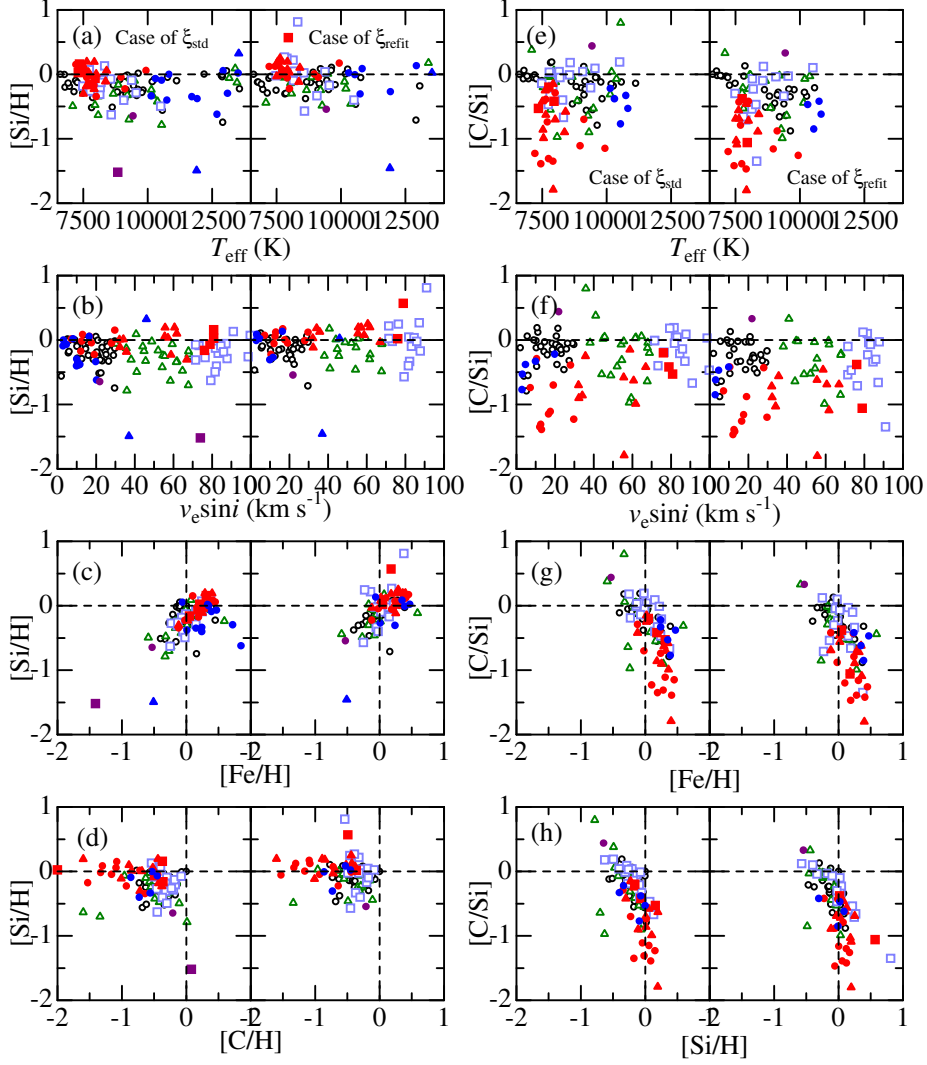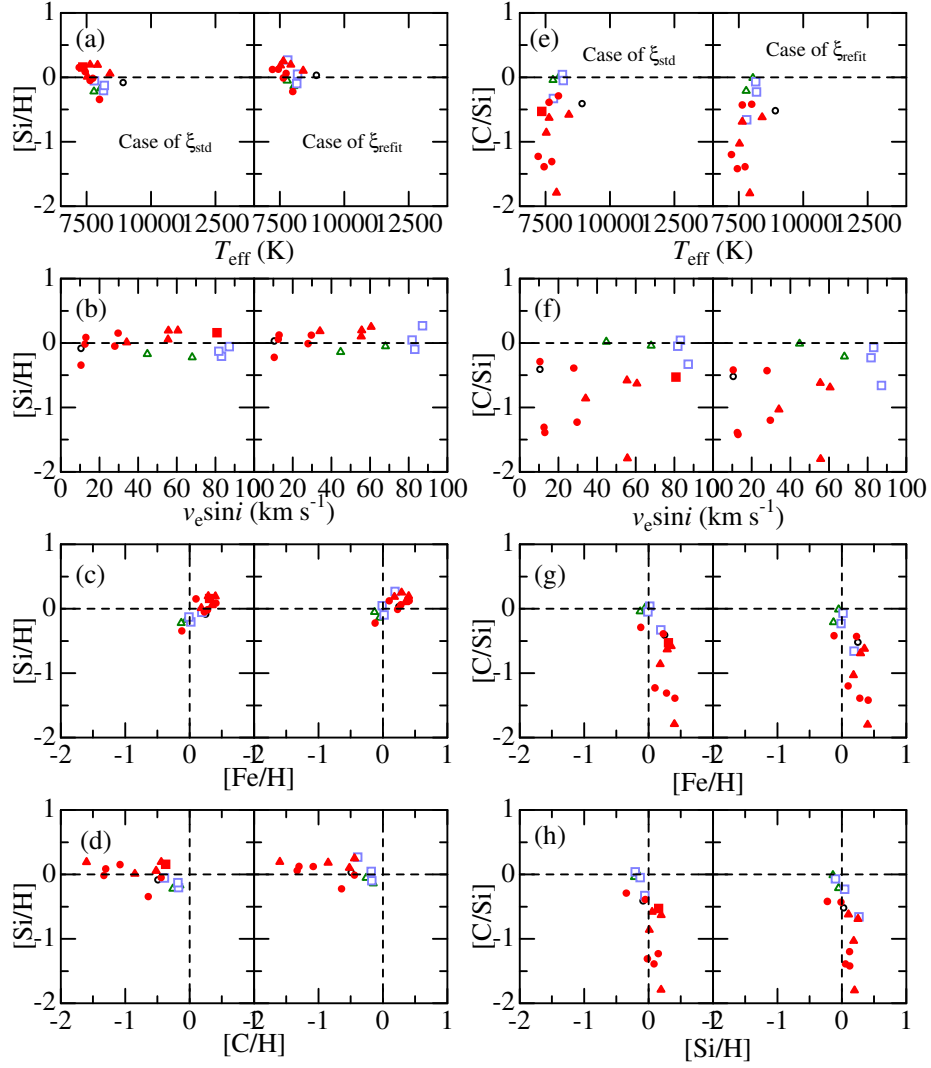
Figure 8. Graphical display of how [Si/H] and [C/Si] for the 120 program stars are related to stellar parameters (or abundances). Left panels: [Si/H] (Si abundance relative to Procyon) plotted against (a) T_{eff}, (b) $v_{\mathrm{e}}\sin i$, (c) [Fe/H], and (d) [C/H]. Right panels: [C/Si] (logarithmic C-to-Si abundance ratio) plotted against (e) T_{eff}, (f) $v_{\mathrm{e}}\sin i$, (g) [Fe/H], and (h) [Si/H]. Each panel consists of two similar diagrams constructed from different Si abundances $A_{\mathrm{std}}^{\mathrm{N}}$ (left) and $A_{\mathrm{refit}}^{\mathrm{N}}$ (right) corresponding to ξ_{std} and ξ_{refit}, respectively. Stars of different $v_{\mathrm{e}}\sin i$ classes are discriminated by the types of symbols: circles ($0 < v_{\mathrm{e}}\sin i < 30\ \mathrm{km\ s^{-1}}$), triangles ($30 \leq v_{\mathrm{e}}\sin i < 70\ \mathrm{km\ s^{-1}}$), and squares ($70 \leq v_{\mathrm{e}}\sin i < 100\ \mathrm{km\ s^{-1}}$). Normal stars are shown by open symbols, while those classified as chemically peculiar are highlighted by filled symbols (red-filled symbols for Am stars, blue-filled ones for HgMn stars, and purple-filled ones for λ Boo stars).

Figure 9. Graphical display of how [Si/H] and [C/Si] for the 16 Hyades cluster stars are related to stellar parameters (or abundances). Otherwise, the same as in Fig. 8.

How can we interpret these results? As mentioned in Section 1, two physical processes may be considered for the possible cause of chemical abundance anomalies: (i) atomic diffusion and (ii) gas–dust separation. Regarding the former diffusion process, although considerable uncertainties still exist, available theoretical calculations predict a deficiency of C, a slight underabundance of Si, and an overabundance of Fe (cf. Richer et al. 2000; Talon et al. 2006). As to the latter gas–dust separation process, Si as well as Fe (both are refractory elements and should behave similarly) are expected to be anti-correlated with C (volatile species).

Although [C/Si] apparently decreases with an increase in [Si/H], this trend can not be simply explained by the gas–dust separation alone, because the (negative) gradient of $d[C/Si]/d[Si/H]$ in Fig. 8h is too steep to be identified with Holweger and Stürenburg's (1993) Fig. 2 (the slope is $\sim -45°$). Actually, the considerably wide range of [C/Si] (~ 2 dex) is mainly due to the diversified deficiency of C ($-1.5 \lesssim [C/H] \lesssim 0$ especially seen in Am stars of lower $T_{\rm eff}$; cf. Fig. 8d) while the contribution of [Si/H] is comparatively minor. Therefore, the main cause of C deficiency is attributed to (not the dust–gas separation but) to atomic diffusion as discussed in T18.

Regarding the cause for the dispersion of [Si/H], the fact that [Si/H] and [Fe/H] correlate well with each other (Fig. 8c, Fig. 9c; just like Holweger and Stürenburg's Fig. 3) may indicate that the gas–dust separation process (acting both Si and Fe in a same direction) is involved at least partly, because atomic diffusion would differently affect Si and Fe according to the currently available calculations. However, it is unlikely that the diffusion process does not play any role in affecting the surface abundances of Si and Fe, since Takeda and Sadakane (1997) reported the $v_{\rm e} \sin i$-dependence of over-/under-abundance of Fe/O in Hyades A-type stars (cf. Fig. 7 therein) which is reasonably interpreted as the result of atomic diffusion being more effective for slower rotators.

Consequently, given the available information alone, it is hardly possible to find any satisfactory interpretation regarding the observed behavior of Si abundances (particularly in relation to the abundances of C and Fe). It may be possible that both processes (atomic diffusion and gas–dust separation) concurrently operate in an intricate manner (the former being more significant?). Unfortunately, the current diffusion calculations appear to still suffer considerable uncertainties (e.g., in the choice of parameters concerning turbulent mixing or mass loss).[6] Further progress in this field is desirably awaited, so that it may shed light to this complicated situation.

---

[6] In this context, Takeda et al. (2012) pointed out that [Na/H] well correlate with [Fe/H] in A-type stars, which contradicts the prediction from the diffusion theory (Na is expected to be almost normal or slightly underabundant unlike Fe). That situation is quite similar to the present case of [Si/H].

References

Aggarwal K. M., Keenan F. P., 2014, MNRAS, 442, 388 (DOI: `10.1093/mnras/stu883`)

Arenou F., Grenon M., Gómez A., 1992, A&A, 258, 104

Cunto W., Mendoza C., 1992, Rev. Mex. Astron. Astrofis., 23, 107

ESA, 1997, The Hipparcos and Tycho Catalogues, ESA SP-1200, available from NASA-ADC or CDS in a machine-readable form (file name: `hip_main.dat`)

Flower P. J., 1996, ApJ, 469, 355 (DOI: `10.1086/177785`)

Ghazaryan S., Alecian G., 2016, MNRAS, 460, 1912 (DOI: `10.1093/mnras/stw911`)

Hoffleit D., Jaschek C., 1991, The Bright Star Catalogue, 5th revised edition (New Haven, Conn.: Yale University Observatory)

Holweger H., Stürenburg S., 1993, in Peculiar Versus Normal Phenomena in A-Type and Related Stars, ASP Conf. Ser. 44, eds. M. M. Dworetsky, F. Castelli, and R. Faraggiana (Astronomical Society of the Pacific: San Francisco), p. 356

Kurucz R. L., 1993a, Kurucz CD-ROM, No. 13 (Harvard-Smithsonian Center for Astrophysics)

Kurucz R. L., 1993b, Kurucz CD-ROM, No. 14 (Harvard-Smithsonian Center for Astrophysics)

Kurucz R. L., Bell B., 1995, Kurucz CD-ROM, No. 23 (Harvard-Smithsonian Center for Astrophysics)

Lejeune T., Schaerer D., 2001, A&A, 366, 538 (DOI: `10.1051/0004-6361:20000214`)

Mashonkina L., 2020a, MNRAS, 493, 6095 (DOI: `10.1093/mnras/staa653`)

Mashonkina L., Ryabchikova T., Alexeeva S., Sitnova T., Zatsarinny, O., 2020b, MNRAS, 499, 3706 (DOI: `10.1093/mnras/staa3099`)

Michaud G., Alecian G., Richer J., 2015, Atomic Diffusion in Stars (Switzerland: Springer International Publishing) (DOI: `10.1007/978-3-319-19854-5`)

Napiwotzki R., Schönberner D., Wenske, V., 1993, A&A, 268, 653

Niemczura E., Murphy S. J., Smalley B., Uytterhoeven K., Pigulski A., Lehmann H., Bowman D. M., Catanzaro G., van Aarle E., et al., 2015, MNRAS, 450, 2764 (DOI: `10.1093/mnras/stv528`)

Preston G. W., 1974, ARA&A, 12, 257
  (DOI: `10.1146/annurev.aa.12.090174.001353`)

Richer J., Michaud G., Turcotte S., 2000, ApJ, 529, 338 (DOI: `10.1086/308274`)

Saffe C., Miquelarena P., Alacoria J., Flores M., Jaque Arancibia M., Calvo D., Martín Girardi G., Grosso M., Collado A., 2021, A&A, 647, A49 (DOI: `10.1051/0004-6361/202040132`)

Takeda Y., 1991, A&A, 242, 455

Takeda Y., 1995, PASJ, 47, 287

Takeda Y., Han I., Kang D.-I., Lee B.-C., Kim K.-M., 2008, JKAS, 41, 83 (DOI: `10.5303/JKAS.2008.41.4.083`)

Takeda Y., Kambe E., Sadakane K., Masuda S., 2010, PASJ, 62, 1239 (DOI: `10.1093/pasj/62.5.1239`)

Takeda Y., Kang D.-I., Han I., Lee B.-C., Kim K.-M., 2009, PASJ, 61, 1165 (DOI: `10.1093/pasj/61.5.1165`)

Takeda Y., Kang D.-I., Han I., Lee B.-C., Kim K.-M., Kawanomoto S., Ohishi N., 2012, PASJ, 64, 38 (DOI: `10.1093/pasj/64.2.38`)

Takeda Y., Kawanomoto S., Ohishi N., 2007, PASJ, 59, 245 (DOI: `10.1093/pasj/59.1.245`)

Takeda Y., Kawanomoto S., Ohishi N., 2014, PASJ, 66, 23 (DOI: `10.1093/pasj/pst024`)

Takeda Y., Kawanomoto S., Ohishi N., Kang D.-I., Lee B.-C., Kim K.-M., Han I., 2018, PASJ, 70, 91 (T18) (DOI: `10.1093/pasj/psy091`)

Takeda Y., Ohkubo M., Sato B., Kambe E., Sadakane K., 2005b, PASJ, 57, 27 (DOI: `10.1093/pasj/57.1.27`)

Takeda Y., Sadakane K., 1997, PASJ, 49, 367 (DOI: `10.1093/pasj/49.3.367`)

Takeda Y., Sato B., Kambe E., Masuda S., Izumiura H., Watanabe E., Ohkubo M., et al., 2005a, PASJ, 57, 13 (DOI: `10.1093/pasj/57.1.13`)

Talon S., Richard O., Michaud G., 2006, ApJ, 645, 634 (DOI: `10.1086/504066`)

van Leeuwen F., 2007, Hipparcos, the New Reduction of the Raw Data, Astrophysics and Space Science Library, Vol. 350 (Berlin: Springer) (DOI: `10.1007/978-1-4020-6342-8`)

A. Non-LTE effects on Si II 6347/6371 lines in B-type stars

Recently, Mashonkina (2020a) carried out an extensive study on the non-LTE line formation for silicon (Si I, Si II, and Si III) in main-sequence stars of A- and B-type covering the $T_{\rm eff}$ range between 7000 and 20000 K. Mashonkina's calculation includes the Si II 6347/6371 lines and the non-LTE corrections for these lines derived by her for late A through late B stars ($T_{\rm eff} \sim$ 7000–13000 K; negative Δ with extents of several tenths dex) are more or less consistent with the results of this investigation.

However, her calculation failed to explain the formation of these Si II doublet lines in the early B-type star ι Her ($T_{\rm eff} =$ 17500 K), because of the *positive* non-LTE corrections resulting in unacceptably large non-LTE Si abundances ($\Delta_{6347} = +0.60$, $\Delta_{6371} = +0.67$, $A_{6347}^{\rm N} = 8.38$, $A_{6371}^{\rm N} = 8.27$; cf. Table 4 in her paper).

Although such an early B-type star is outside of the scope of this study, it is interesting to examine whether similar inconsistency emerges in our calculations at the higher $T_{\rm eff}$ regime ($>$ 15000 K). For this purpose, additional non-LTE calculations were performed for the $\log g = 4$ models with extended $T_{\rm eff}$ up to 20000 K. The resulting runs of $l_0^{\rm NLTE}/l_0^{\rm LTE}$ and $S_{\rm L}/B$ with depth for the Si I 6347/6371 lines (from $T_{\rm eff} =$ 8000 K through 20000 K) are depicted in Figs. 10a and 10b; and Figs. 10c and 10d display how W_{6371} and Δ_{6371} (for the weaker line of the doublet) vary with $T_{\rm eff}$.

Our calculations suggest that the extent of the (negative) non-LTE abundance correction ($|\Delta|$) progressively decreases with an increase of $T_{\rm eff}$ in the regime of B-type stars ($T_{\rm eff} \gtrsim$ 10000 K), until it eventually reaches $\Delta \sim 0$ at the critical $T_{\rm eff}$ of $\sim$ 19000 K; thereafter Δ turns into positive (cf. Fig. 10d). In other words, the line is strengthened by the non-LTE effect ($W^{\rm N} > W^{\rm L}$) at $T_{\rm eff} \lesssim$ 19000 K while weakened ($W^{\rm N} < W^{\rm L}$) at $T_{\rm eff} \gtrsim$ 19000 K, as can be confirmed in Fig. 10c.

As mentioned in Section 6.1, the behavior of Δ is mainly controlled by the line source function; that is, as long as the inequality $\langle S_{\rm L} \rangle < \langle B \rangle$ ($S_{\rm L}$ dilution) holds in the line-forming region, Δ remains negative. However, according to Fig. 10b, as $T_{\rm eff}$ is ever increased, $\langle S_{\rm L} \rangle$ becomes comparable with or even outweighs $\langle B \rangle$, which explains why Δ approaches zero or even turns into positive at higher $T_{\rm eff}$ ($\sim$ 20000 K).

Fig. 10d suggests that the non-LTE correction for ι Her ($T_{\rm eff} =$ 17500 K) expected from our calculation is $\Delta_{6371} \sim -0.1$ dex, Then, since the LTE abundance is $A_{6371}^{\rm L} =$ 7.60 (cf. Table 4 in Mashonkina 2020a), the non-LTE Si abundance for ι Her would make $A_{6371}^{\rm N} \sim 7.5$, which is almost consistent with the solar abundance.

Mashonkina's (2020a) Δ_{6371} vs. $T_{\rm eff}$ relation (taken from Table 9 of her paper) is also overplotted for comparison in Fig. 10d. We can see from this figure that the upturn of Mashonkina's Δ_{6371} is considerably steeper and $\Delta_{6371} \sim 0$ is attained already at $T_{\rm eff} \sim$ 13000–14000 K, which is in marked contrast to our calculation (critical $T_{\rm eff}$ for $\Delta_{6371} \sim 0$ is at $\sim$ 19000 K). The reason for this discrepancy is not clear. An inspection of the bottom panel of Mashonkina's (2020a) Fig. 1 (in comparison with our Fig. 10a) suggests that Si II levels are largely underpopulated (presumably due to more enhanced Si II overionization) in her calculation. We suspect that her procedure of evaluating UV photoionizing radiation field may have been rather different, for which we used the opacities included in Kurucz's (1993a) ATLAS9 program along with Kurucz's (1993b) line opacity distribution function as described in Section 3.1.2 of Takeda (1991).
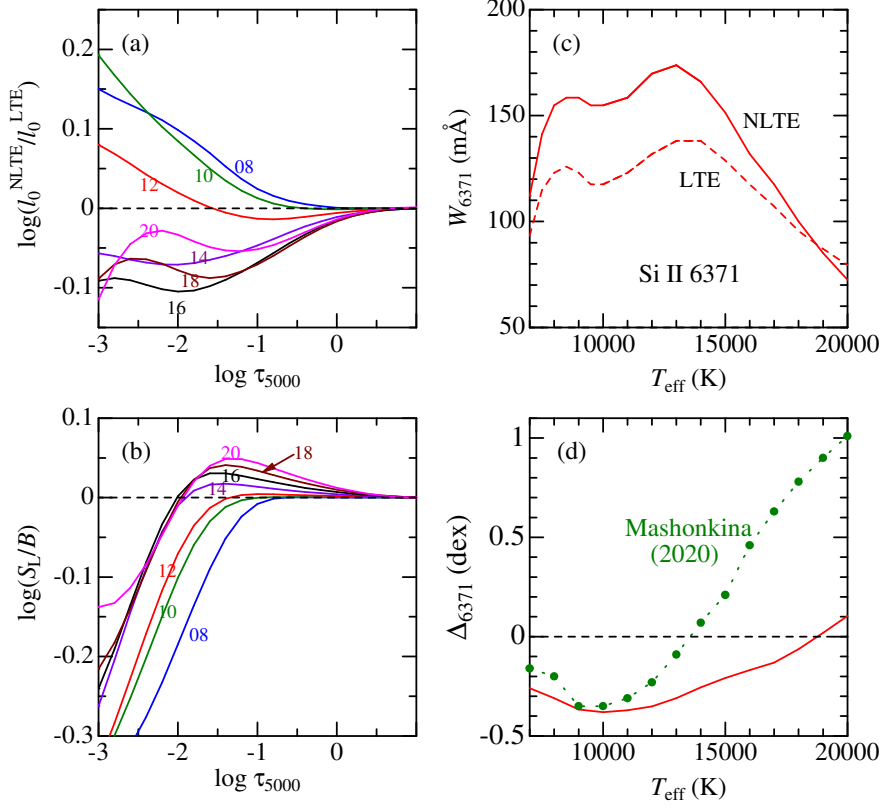
Figure 10. Non-LTE calculation results for the Si II 4s ^{2}S–4p ^{2}P$^\circ$ transition of multiplet 2 (like the case of Figs. 5 and 6), which were derived for $\log g = 4$ models (with $\xi = 2$ km s^{-1} and [Si/Fe] = [Fe/H] = 0) but T_{eff} extended up to 20000 K (in order to cover early B stars). (a) The non-LTE-to-LTE line-center opacity ratio (vs. τ_{5000}), (b) S_{L}/B ratio (vs. τ_{5000}), (c) non-LTE and LTE equivalent widths for Si II 6371 (vs. T_{eff}), and (d) non-LTE correction for Si II 6371 (vs. T_{eff}). In panels (a) and (b), $T_{\mathrm{eff}}/1000$ is marked in each curve. In panel (d), the T_{eff}-dependence of Δ_{6371} calculated by Mashonkina (2020a) is also shown for comparison.